ACS OMEGA

Open Access

http://pubs.acs.org/journal/acsodf

Article

Efficient Standalone Flexible Small Molecule Organic Solar Cell Devices: Structure-Performance Relation Among Tetracyanoquinodimethane Derivatives

Anuradha Mohitkar, Renuka H, Sanket Goel, and Subbalakshmi Jayanty*

Cite This: *ACS Omega* 2023, 8, 40836−40847

Read Online

ACCESS | Metrics & More | Article Recommendations | Supporting Information

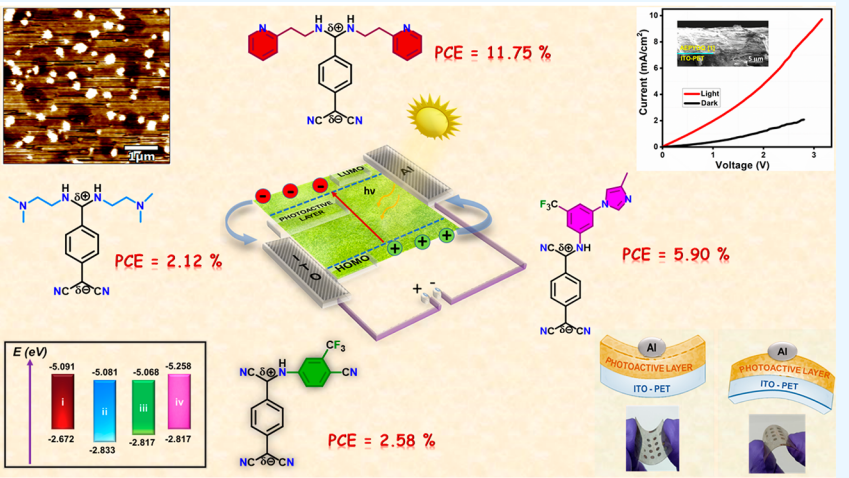

ABSTRACT: Currently, very few dicyano and tetracyanoquinodimethane (TCNQ) based molecules are utilized as active layers, sandwiched between the electron and hole transport layer in organic solar cell (OSC) devices. Nevertheless, simple mono- and disubstituted TCNQ derivatives as exclusively active layers are yet unexplored and provide scope for further investigation. In this study, TCNQ derivatives with varying amine substituents, namely, AEPYDQ (**1**), BMEDDQ (**2**), MATBTCNQ (**3**), and MITATCNQ (**4**), were explored as efficient standalone, flexible, all small molecule OSC devices. Particularly, **1** resulted in the highest device efficiency of 11.75% with an aromatic amine, while **2** possessing an aliphatic amine showed the lowest power conversion efficiency (PCE; 2.12%). Notably, the short circuit current density (J_{SC}) of device **1** increased from 2 mA/cm^2 in the dark to 9.12 mA/cm^2 under light, indicating a significant boost in the current generation. Further, **1** manifested more crystallinity than others. Interestingly, **4** exhibited a higher PCE (5.90%) than **3** (PCE is 2.58%), though **3** is disubstituted with an aromatic amine, probably attributed to the electron-withdrawing effects of the $-CF_3$ and $-CN$ groups in **3** reducing the available π-electron density for stacking. Therefore, this study emphasizes crystallinity, significantly on the PCE, offering insights into the design of many such efficient OSCs.

1. INTRODUCTION

Being a stronger π-electron acceptor, tetracyanoquinodimethane (TCNQ) experiences a nucleophilic substitution reaction when reacted with primary/secondary amines, resulting in predominantly substituted/cyclized derivatives popularly termed diaminodicyanoquinodimethanes (DADQs).[1] Intramolecular charge transfer (ICT) occurs in this D−π−A framework across the π system, and variation in amine substituent DADQs displays captivating and unpredictable properties. This distinctive nature of DADQs allows them to fine-tune their structure, enabling them to exhibit diverse applications. Hence, DADQs have been used with respect to optical,[1−3] nonlinear optical,[4,5] semiconducting,[6−9] and mechanochromic[10−12] materials, and as molecular hopper crystals.[13] However, the utilization of TCNQ-based compounds in optoelectronics is very limited. Incidentally, OSCs retain remarkable features compared to polymer counterparts, for instance, simple design, low cost, light weight, and flexibility, paving the way for their commercialization in

Received: August 12, 2023
Revised: October 3, 2023
Accepted: October 4, 2023
Published: October 22, 2023

https://doi.org/10.1021/acsomega.3c05939
ACS Omega 2023, 8, 40836−40847

Scheme 1. Synthetic Strategies for the Formation of 1−4[a]

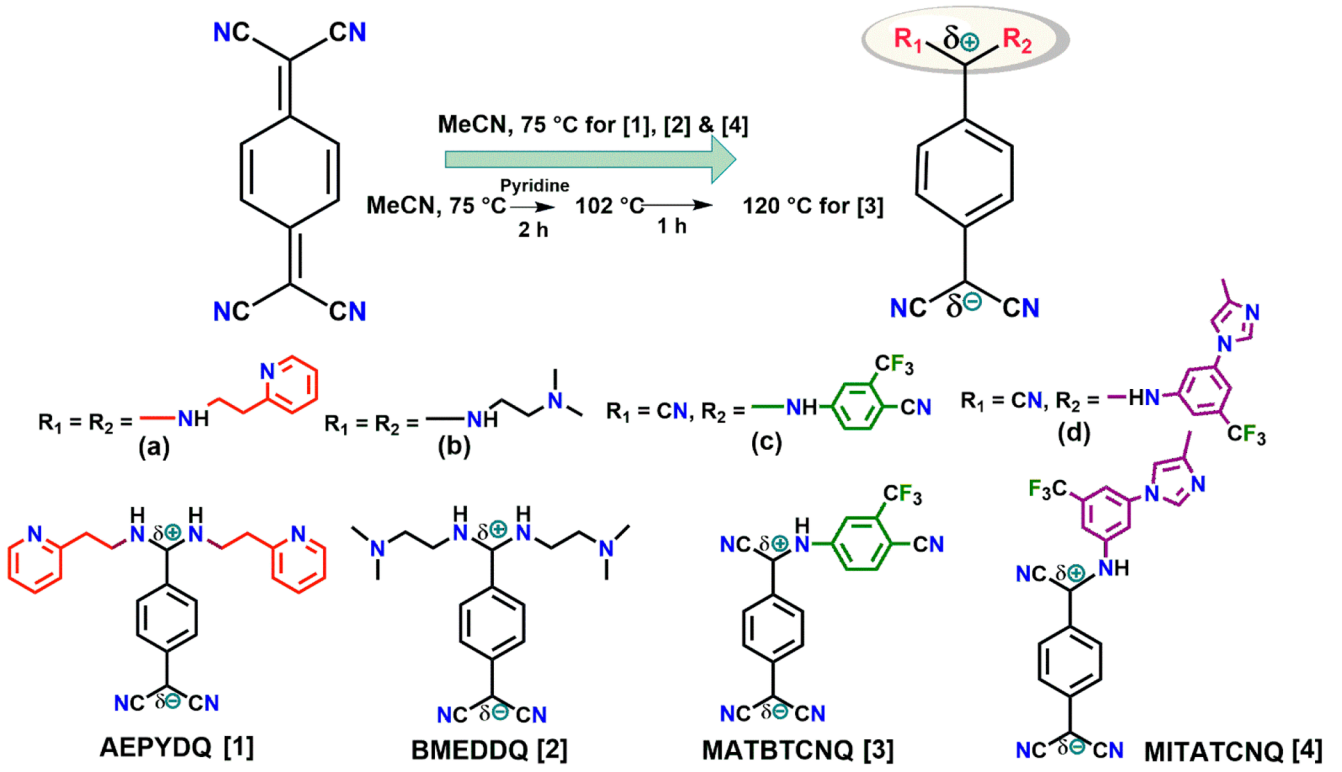

[a]a, b, c, and d were reacted with TCNQ to attain **1**, **2**, **3**, and **4**, respectively. While **1**, **2**, and **4** were obtained by adding a, b, and d at ∼75 °C to the acetonitrile (MeCN) solution of TCNQ, respectively, **3** was achieved by adding a catalytic amount of pyridine as well, after the addition of c to the MeCN solution of TCNQ, and further increasing the temperature up to ∼120 °C.

portable and flexible green energy harvesting devices.[14,15] Progression in optoelectronics revealed that organic-material-based platforms in their photovoltaic (PV) applications are potent enough to surpass Si-based devices. Recently, organic solar cells (OSCs) have been capable of achieving a power conversion efficiency (PCE) of about 20% by means of interfacial and epitaxial engineering of bulk heterojunctions (BHJ).[16,17] Despite this, lower output potentials and active layer instability have hampered the commercialization of tandem structures. Also, considerable efforts have been attenuated since it is difficult to forecast the accompanying qualities of organic synthesis, sparing ample resources and producing many products that work poorly or in no way. Therefore, concomitantly, it is essential to conduct systematic investigations to develop economic, simple, yet highly efficient and stable PV cells.

A theoretical study of an imidazolidine moiety prototype with a linked diamino methylene group was proposed for a solar cell application;[18] however, it has not been isolated or characterized structurally. Introducing TCNQ as acceptor and peripheral donor groups as *m*-dimethoxy phenyl, phenyl, *N*,*N*-dimethylaniline, and triphenylamine moieties achieved a lower band gap of 0.52−1.46 eV along with higher thermal stability, enabling their usage for organic optoelectronic devices.[8] Furthermore, organic field-effect transistors developed from benzothieno[3,2-*b*][1]benzothiophenes (BTBT) and fluorinated TCNQs were characterized electronically as active layers within thin film devices.[9] Recently, p-type doping of F4-TCNQ in the hole transport layer of spiro-OMeTAD resulted in improved stability and carrier lifetime of perovskite solar cells.[19] The above reports indicate that TCNQ derivatives possibly with aromatic amine substituents could accord promising optoelectronic effects.

Recently, we introduced the solar cell application of BCCPDQ (1-cyclopropyl carbonyl piperazine as an amine substituent on TCNQ), which, when combined with a TiO_2 nanoparticle layer, displayed an improved power conversion efficiency (PCE), i.e., 2.26% compared to the standalone device comprised of pristine BCCPDQ. This encouraging outcome motivated us to explore the photovoltaic application of additional TCNQ derivatives, paving the path toward developing standalone devices of all small molecule organic solar cells. Notably, herein the intermediate core when linked with a C−C single bond reduces synthetic complexity and makes it commercially feasible.[16] With the gaining importance of push−pull chromophores, besides D−π−A set up for small molecule organic solar cell (SMOSC) features, fine-tuning the optoelectronic properties with structural alteration motivates us to utilize TCNQ derivatives for SMOSC.

In this article, we considered 7,7-bis (2-(2-aminoethyl)-pyridino)-8,8-dicyanoquinodimethane (AEPYDQ; **1**), 7,7-bis-(*N*,*N*-dimethylethylenediamino)-8,8-dicyanoquinodimethane (BMEDDQ; **2**), 7-(3-amino-5-(trifluoromethyl)benzonitrilo)-7-cyano-8,8 dicyanoquinodimethane (MATBTCNQ; **3**), and 7-(3-(4-methyl-1H-imidazol-1-yl)-5-(trifluoromethyl)anilino)-7-cyano-8,8 dicyanoquinodimethane (MITATCNQ; **4**) as active layers in the fabricated flexible standalone solar cell devices, further establishing a structure−performance relation. To the best of our knowledge, **1**−**4** molecules as active layers considered in this study are the only photoactive materials

https://doi.org/10.1021/acsomega.3c05939
ACS Omega 2023, 8, 40836−40847

among any other TCNQ derivatives attained in a single-step synthesis along with appreciable PCEs. Previous reports on TCNQ-related molecules were obtained either by tedious synthetic procedures or as TCNQ adducts (Table S1). Generally, in all SMOSC-based devices the donor and acceptors were considered individually during device fabrication. Alternatively, in the ternary OSC devices, the active layers are either commercially available polymers or modified polymers resulting in a PCE of up to ∼20%. Nevertheless, in the present study, the donor−acceptor framework is maintained in a single molecule of a TCNQ derivative, i.e., in all **1** to **4**; further, a PCE of 11.75% could be attained in **1**. Primarily, in our previous reports, **1** was studied especially with a second harmonic generation (SHG) perspective and manifested an SHG of ∼6U;[5] similarly **2** on complexation with terephthalic acid generated moderate SHG activity of ∼9U.[20] However, in recent times, **2** exhibited an appreciable fluorescence property with a quantum yield (Φ_f) = ∼0.4% in solution and a Φ_f of ∼50% in a solid. Further, **3** and **4** each possess strong electron-withdrawing groups, an induced redshift, and a large Stokes shift of ∼126 and 152 nm, respectively.[21] Nevertheless, the photophysical property of **1** is yet unrevealed. Herein, four TCNQ derivatives containing secondary amine substituents are considered; notably **1** and **2** are disubstituted TCNQ derivatives with **1** comprising an aromatic amine and **2** an aliphatic amine, while **3** and **4** are monosubstituted TCNQ derivatives, with both **3** and **4** having aromatic amines with electron-withdrawing groups. Additionally, **4** has extended π-electron conjugation in relation to **1**. Consequently, this article describes a detailed fluorescence study of **1** followed by a comprehensive investigation of the device fabrication and, especially, the solar-cell potential of **1**−**4** intimating the influence of structure on the PCE. Further, although the spin-coating technique is often used due to its simplicity, and affordable fabrication, it also suffers from high-density pinholes that reduce the PCE and a greater volume of precursor solution required;[22] alternately drop-casting is known to retain film quality, provide greater crystallinity and substantially better resistance to humidity than spin-coating,[23] and provide improved $J-V$ performance.[24] Suitably, this work focuses on drop-casted films for consistent surface covering, rapid production, and minimal material consumption. The stability of the devices is mainly related to changes in the fill factor (FF) over time, and we relate these changes to the structure, morphology, and photoexcitation of the light-harvesting layer. This work showcases the pivotal features in designing TCNQ derivative-based active layers for achieving a higher PCE.

2. EXPERIMENTAL SECTION

2.1. Methodology. The synthesis of **1**, **2**, **3**, and **4** was done by modifying the reported procedure.[5,21] The entire instrumental description for characterization and spectroscopic studies is discussed in the Materials, Measurements, and Characterization in the Supporting Information (SI). Synthetic strategies for the formation of these compounds are highlighted in Scheme 1.

2.2. Fabrication Process. Spin-coated films at 300 rpm for 1 min (optimized) for **1**−**4** resulted in small region occupancy with nonuniform deposition on the substrate, which was inadequate to facilitate proper contacts in order to conduct PV measurements; therefore, the drop-casting method was contemplated. Comparative representative pictures related to the spin coating and drop casting for **1** are shown in Figures S1 and S2. Fabrication of the ITO-PET/(**1**/**2**/**3**/**4**)/Al PV device was accomplished by drop casting 3 mM DMF solutions of **1**, **2**, **3**, and **4** on indium tin oxide (ITO) coated polyethylene terephthalate (PET; bottom substrate/cathode) each individually, heated at 60 °C for 5 min with additional drying for 60 min at room temperature (Figure S3). Aluminum (Al) acting as the top electrode had been deposited by a masking procedure with e-beam evaporation. **1**, **2**, **3**, and **4** were insoluble in chloroform ($CHCl_3$) and dichloromethane (DCM). While **1** and **2** had appreciable solubility in MeOH and ethanol EtOH, **3** and **4** were soluble in methanol (MeOH) and ethanol (EtOH) under heating. **1** and **2** were highly soluble in acetonitrile (MeCN); **3** and **4** were dissolved in MeCN on heating. However, **1**−**4** were immediately soluble in dimethylformamide (DMF), making it the most suitable solvent for thin film studies. Hence, all of the thin films prepared in DMF as **1**, **2**, **3**, and **4** are highly soluble and finely coated on the ITO-PET substrate. Further, all of the films were studied by atomic force microscopy (AFM), field emission scanning electron microscopy (FESEM), and transmission electron microscopy (TEM). The thickness of the films was 5 μm (**1**), 2.1 μm (**2**), 1.5 μm (**3**), and 3.1 μm (**4**) individually. For determining the electrical characteristics of the standalone organic PV cell, the source measurement tool (Keysight B2912A) was operated by applying a potential bias in the range of −3 to +3 V. The samples were exposed to the uniform light of 1 Sun (Am 1.5 G, 100 mW/cm^2), emanating from a solar simulator (model #SS0AAA).

3. RESULTS AND DISCUSSION

3.1. Photophysical Properties. The absorption and emission wavelengths for **1**, **2**, **3**, and **4** in DMF are shown in Table S2. Photophysical properties of **2**, **3**, and **4** have been described by us very recently.[5,21] However, the fluorescence property of **1** has not yet been reported. Therefore, herein, we report the detailed photophysical characteristics of **1**. The lowest energy absorption among **1**−**4** indicates the characteristic feature of intramolecular charge-transfer transition.[25−28] Lower wavelength absorption in **1** and **2** specifies a more polar ground state. Larger Stokes shifts (∼160 nm) in **3** and **4**, i.e., 165 and 154 nm in each, compared to **1** and **2** (∼88 nm) suggest a change in dipole moment among the ground and excited states, in a polar environment,[28] thereby possessing photostability due to good separation of the excitation and emission light. Table S3 presents the absorption and emission study of **1** in solution and as a solid. λ_{max} emission was found to be alike (∼470 nm) in all of the solvents considered, except MeCN (∼428 nm), indicating emission arising from a similar locally excited state in the solvents except MeCN.[26,28] A blue shift (∼42 nm) observed in λ_{max} emission in MeCN could be due to constricted nonradiative decay of the excited state in MeCN, leading to stabilization. Further, enhanced fluorescence emission was noted in the DMF solution (Φ_f ∼ 0.46%) of **1** than that in the solid form (Φ_f ∼1.22%; Figure S4a); nevertheless, a larger Stokes shift in the former indicates more vibrational relaxation of the excited states. The chromaticity diagram (Figure S4b) revealed a blue color emitted in the solid **1** with color coordinates as X = 0.127 and Y = 0.446. Fluorescence lifetime decay (τ) of DMF solutions in **1** was 0.032 ns (Figure S4c); **2** exhibited τ = 2.04 ns; **3** and **4** displayed ∼0.07 and ∼0.22 ns, respectively. The excited state's rapid relaxations by a nonradiative decay path were observed in

https://doi.org/10.1021/acsomega.3c05939
ACS Omega 2023, 8, 40836−40847

1 and **3**. Multiple exponentials and chi-square (χ^2) values determined the fitting accuracy (Table S4). Solids **1** and **2** under excitation wavelengths of 410 and 380 nm, respectively, show comparable lifetimes, i.e., 0.88 and 1.2 ns, sequentially, suggesting the presence of multiple conformations in excited states, i.e., **1** relaxed through four decay channels and **2** through three decay channels. A considerable fluorescence lifetime was not displayed by solids **3** and **4** due to rapid excited state relaxation by the nonradioactive decay pathway. The solvent effect hinders the excited relaxation in solutions as opposed to solids. **1**−**4** coated on a ITO-PET substrate individually absorbed light in the UV−visible region (Figure 1).

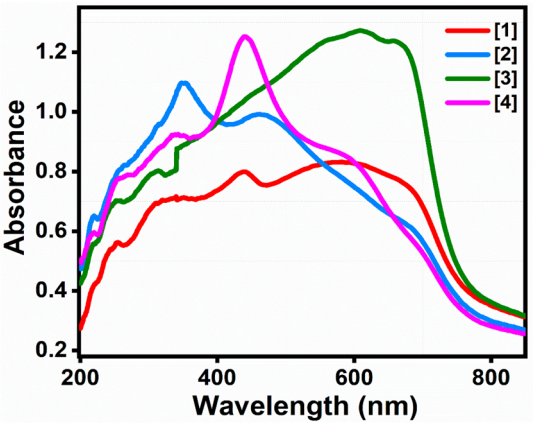

Figure 1. Absorption spectra for films **1**−**4** coated in ITO-PET manifesting broad absorption suggestive of strong intermolecular interactions.

In all of the films, the observed redshift compared to solutions indicates adequate aggregation of molecules and $\pi-\pi$ interaction in the solid state. Moreover, the broader absorptions with significant shifts seen in the solutions (Figure S5) point toward stronger intermolecular interactions along with the existence of exciton coupling effects within the films.[26]

3.2. Electrochemical Studies. Electrochemical behavior was executed by cyclic voltammetry (CV) to measure the energy levels in **1**−**4**. 0.1 M tetrabutylammonium perchlorate (0.1 M) in MeCN was considered to constitute 6 μM **1**−**4** solutions at a 25 mV s^{-1} scan rate (Figure 2a, Figures S6a−S8a). Scan rate-dependent studies were examined by varying scan rates from 10 mV s^{-1} to 100 mV s^{-1} (Figure 2b, Figures S6b−S8b). Three quasi-reversible reduction waves for **1** ($E_{1/2}$ at −0.04 V, −1.32 V, −2.14 V); **3** ($E_{1/2}$ at −0.56 V, −1.26 V, −1.81 V; vs Ag/AgCl); and **4** ($E_{1/2}$ at −1.31 V, −1.88 V, −2.28 V) were seen; on the contrary, **2** ($E_{1/2}$ at −1.33 V, −1.86 V) showed two quasi-reversible reduction waves; this signifies consecutive three reductions of dicyanomethylene end turning into the corresponding radical anions[29] for **1**, **3**, **4**; whereas two consecutive reductions of the same for **2**. Additionally, the donor (amine) functionality reports three irreversible oxidation peaks for **1** (E^{ox} at −0.63 V, 0.48 V, 0.99 V), **3** (E^{ox} at −0.87 V, 0.24 V, 0.53 V), and **4** (E^{ox} at −1.28 V, −0.92 V, 0.48 V) and two irreversible oxidation peaks for **2** (E^{ox} at −0.84 V, 1.91 V). The highest occupied molecular orbital (HOMO) and lowest unoccupied molecular orbital (LUMO) energy levels and the associated bandgap were calculated from the empirical equations mentioned below:[30]

$$E_{LUMO} = -[E^{Red}_{onset} - 0.49 + 4.8]\ \text{eV and}$$

$$E_{HOMO} = -[E^{ox}_{onset} - 0.49 + 4.8]\ \text{eV}$$

$$\text{Band Gap} = E_{LUMO} - E_{HOMO}$$

Using the aforementioned equation, the electrochemical band gap is calculated as ∼2.3 eV, a typical semiconductor

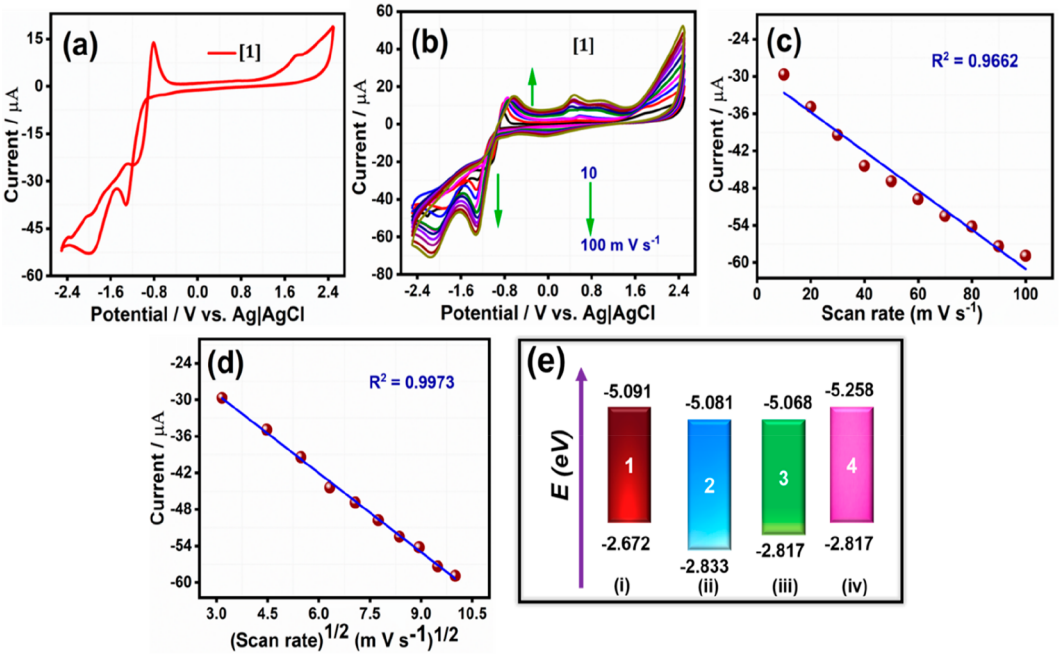

Figure 2. (a) Cyclic voltammogram of **1** in dry MeCN at a 25 mV s^{-1} scan rate with supporting electrolyte. (b) Scan-rate-dependent cyclic voltammogram of **1** with scan rate sweeping from 10 to 100 mV s^{-1}. (c) Cathodic peak current altered with scan rate. (d) Response of cathodic peak current to the scan rate root square, and (e) energy levels of (i) **1**, (ii) **2**, (iii) **3**, (iv) **4**.

https://doi.org/10.1021/acsomega.3c05939
ACS Omega 2023, 8, 40836−40847

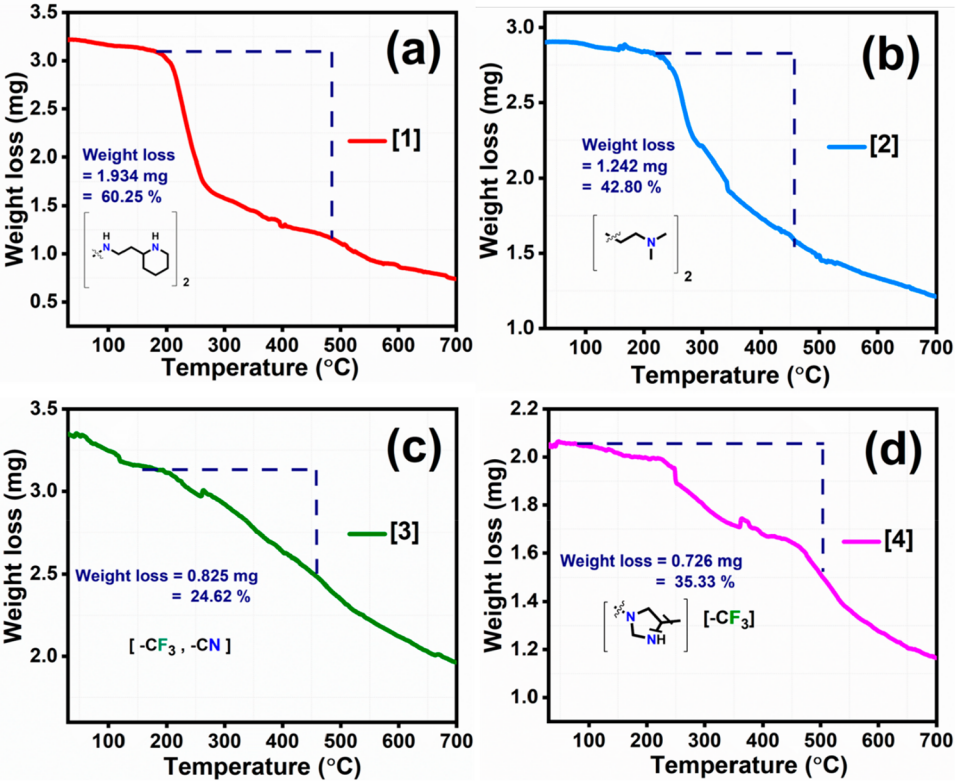

Figure 3. Thermogram for (a) **1**, (b) **2**, (c) **3**, and (d) **4**.

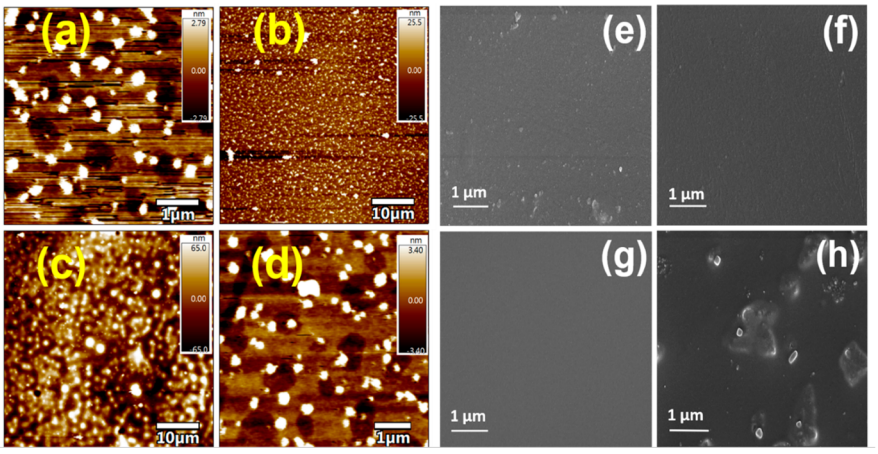

Figure 4. AFM images with height profile in the inset of (a) **1**, (b) **2**, (c) **3**, and (d) **4** reveal a crystalline nature. FESEM images of (e) **1**, (f) **2**, (g) **3**, and (h) **4** also show microcrystalline aggregates.

range for each **1**−**4**. Further, to understand the mechanism followed through the electrochemical process, the samples scan rate-dependent study was performed. Generally, the redox process follows two perspectives; i.e., if the scan rate is proportional to the anodic/cathodic peak current, the rate-determining step depicts the electron transfer process. Contrarily, diffusion of counterions becomes the rate-determining step when the peak current is proportional to the square root of the scan rate.[31,32] Accordingly, **1**−**4** followed the diffusion-controlled redox process as the cathodic peak current fits better with the square root of the scan rate (Figure 2c,d; Figures S6c,d, S8c,d).

The optical band gap was estimated utilizing the Kubelka−Munk method, where $K = (1 - R)^2/2R$, a Kubelka−Munk factor, R is % reflectance, and E is incident radiation energy. By extrapolating the lines, the point of intersection determines the optical band gap at ∼2.0 eV (Figure S9) among **1**−**4**, which also suggests enhanced ICT. A slight variation among the optical band gap and the electrochemical counterparts is possible, because the bulk effects are neglected at electrodes in the latter. A decrease in optical band gap with extended π conjugation is perceived (Figure 2e). Deep HOMO energy levels (Table S5) are noticed, perhaps affording a higher V_{oc}.[14]

3.3. Thermal Stability. The thermal stabilities of **1**−**4** were evaluated by thermogravimetric analysis (TGA). **1** is stable up to ∼210 °C and later decomposed with a single step, possessing weight loss of 60.25% (1.934 mg; Figure 3a). This weight loss corresponds to two 2-(2-aminoethyl)pyridine

https://doi.org/10.1021/acsomega.3c05939
ACS Omega 2023, 8, 40836−40847

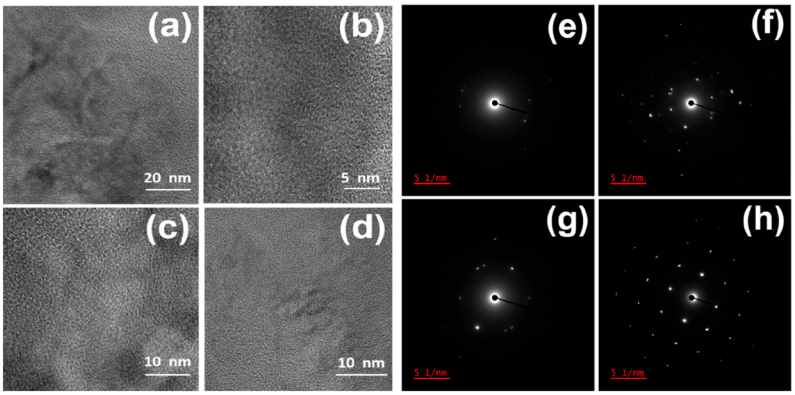

Figure 5. TEM images of (a) **1**, (b) **2**, (c) **3**, (d) **4** and electron diffraction patterns of (e) **1**, (f) **2**, (g) **3**, (h) **4** in MeCN solvent.

moieties. A similar trend to that of **1** was followed by **2** with a weight loss of 42.80% (1.242 mg) owing to the loss of two *N*,*N*-dimethylethylenediamine moieties (Figure 3b). **3** and **4** do not follow the above trend; rather, multistage decomposition with no stable intermediate formation is noticed (Figure 3c,d).

3.4. Morphology Study. For a keen understanding of captivating device performance; the morphology of thin films was contemplated by AFM and FESEM instead of TEM. The crystalline nature of the film is depicted by all four compounds **1**−**4** in AFM (Figure 4a−d). An uneven feature was observed for the films of **2** and **3** at 1 μm (Figure S10), and hence, 10 μm images were captured for the same.

The roughness attained from AFM images shows the crystallinity of the film surface. Root mean square roughness (R_q) for **1** was noticed to be the highest with 19.40 nm, followed by **4** (R_q = 18.36 nm), in good agreement with AFM images. **3** holds weaker crystallinity with R_q = 14.83 nm, and **2** showed the lowest R_q = 8.686 nm. Higher values of R_q highlight the bigger crystallites predominant in **1** and **4** compared to those in **3** and **2**. Generally, surface roughness is correlated with crystallinity features.[33] The FESEM images (Figure 4e−h) also illustrate evenly distributed crystalline facets in **1** and **4** films; further, in **1**, an array of fibrous appearances was noticed (Figure S11) as well. A fibrous surface is known to facilitate efficient charge transport resulting in a high J_{SC}.[34] **2** and **3** emerge with a smooth film formation with smaller crystallites that probably to a certain extent could reduce effective donor−acceptor interaction, lowering the charge generation efficiency. Mostly, all small molecule and polymer OSCs show an R_q (for roughness) around 0.2−1 nm, but herein, R_q ranges from ∼8 to 20 nm, which is relatively high. Such higher values are perceived in perovskite solar cells.[35,36] Though higher R_q values also contribute to the cracked surface of films,[37] nevertheless, in this study, R_q values are attributed to the crystalline nature of films.[33] Moreover, microscopic images manifest uniform, crack-free, and yet smoother film formation.

TEM images were recorded in MeCN (Figure 5a-5d) since in DMF the images were unclear for all three samples except **1**. The crystalline fibrous feature was observed in the DMF (Figure S11) solution-coated film of **1**. At higher resolutions the samples were getting degraded; therefore, images were taken at different magnifications. Besides poor separation of phase is observed in **2** and **3** agreeing with the FESEM information. The selected area electron diffraction (SAED) pattern depicts a higher electron diffraction in **4** followed by **2**, **3**, and **1** (Figure 5e−h). Analysis of the single crystal structure revealed that **1** pertained to the noncentrosymmetric space group, $P2_12_12_1$. Appealingly, there were stronger intermolecular hydrogen bonds (H-bond) among N5−N1 (2.942 Å) and N3−N4 (2.911 Å) and a noncovalent interaction within the H-bond regime N5−N6 (3.094 Å). One among the 2-(2-amino ethyl) pyridine moieties was twisted, generating an intramolecular H-bond as well as an intermolecular H-bond with the CN end of other disubstituted molecules, directing a distinct fashion of molecular dipole orientation, arresting from antiparallel alignment (resulting in SHG activity; Figure S12a). Therefore, in **1**, supramolecular self-assemblies are pronounced to a greater extent owing to the noncovalent interactions and short contact existence, in addition to the presence of H-bonds.[5] **2** belonged to the $P2_1/c$ space group. Molecular dipoles were aligned in antiparallel orientation, disclosing interchain interactions and minimal noncovalent interactions, and supramolecular assemblies were not noticed among the molecular dipoles in **2**.[20] **3** could be attained as a microcrystalline powder and attempts for a single crystal were in vain, despite several efforts.[21] **4** pertained to the $P2_1/c$ space group with dipoles organized in an antiparallel fashion. Though noncovalent intermolecular interactions (∼2.70 to 3.23 Å) were dominant in **4**, stronger H-bonding was seen among N2···H6 (1.950 Å); further, **4** exhibited supramolecular assemblies as well (Figure S12b).[21] The PXRD pattern showed sharp and intense peaks for all **1**−**4**, confirming crystalline attributes (Figure S13).

3.5. Photovoltaic Application. To fully understand how divergent amine substituents impact the device performance, the synthesized **1**−**4** were systematically investigated for photovoltaic behavior under conventional test settings (irradiance 1 sun, AM 1.5 G spectrum). The current density vs voltage curves were acquired in the presence as well as the absence of light illumination. Until the forward bias voltage (V_{FB}) exceeds the open circuit voltage (V_{OC}), there is essentially a small amount of current in the dark. The PV devices begin to produce power when they are illuminated, and this power is measured by a source measuring unit.[31] For any given PV cell, the key characterizing factor is the PCE, which is the ratio of the maximum output power (P_{out}) generated by the PV device to the total incident power (P_{in}).[31] The fill factor (FF) is characterized as the quotient of the maximum power (P_{MAX}) generated by the solar cell and the product of its open circuit voltage (V_{oc}) and short circuit current (J_{SC}).[38,39] The

https://doi.org/10.1021/acsomega.3c05939
ACS Omega 2023, 8, 40836−40847

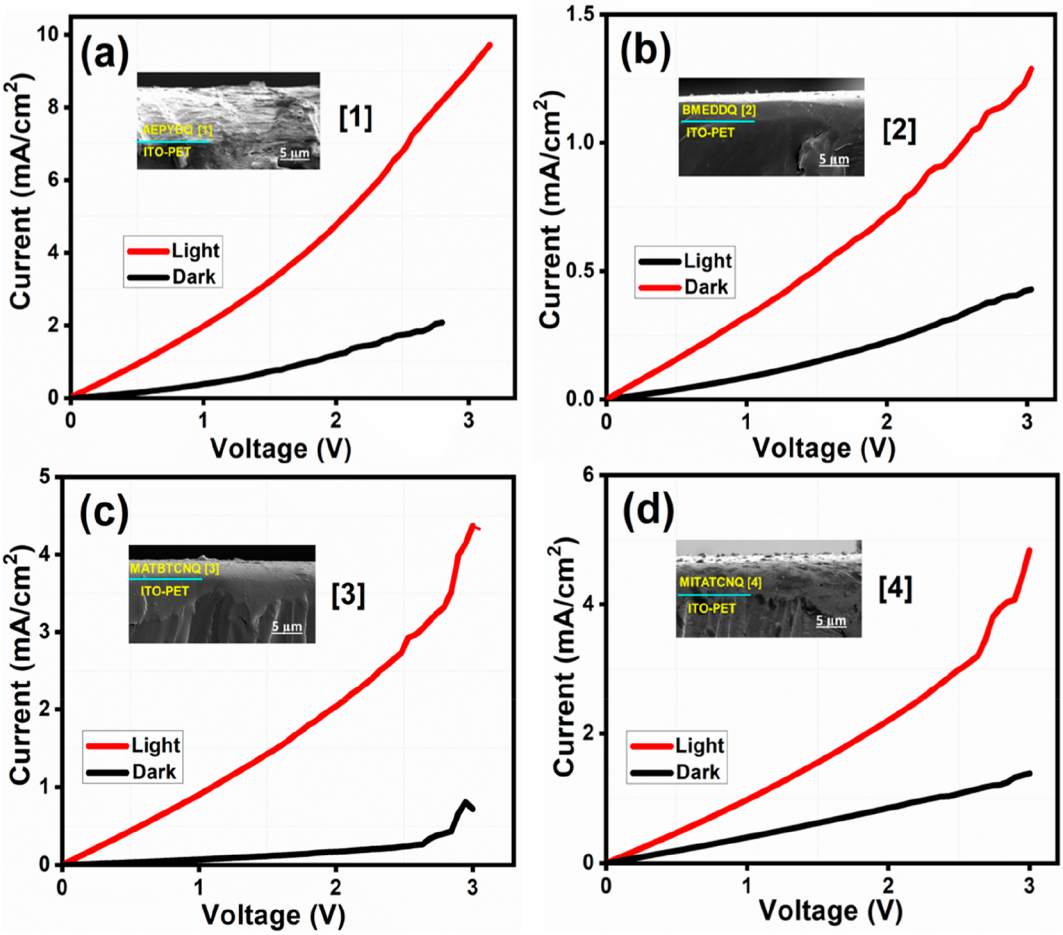

Figure 6. $J-V$ characteristics of (a) **1**, (b) **2**, (c) **3**, and (d) **4** based PV device under dark and light conditions with the cross-sectional microimage in the inset depicting thickness of the photoactive layer of the PV device.

FF serves as an indicator of the ease or difficulty in extracting the photoexcited electron and holes from the PV device.[39,40] The PCE for all the fabricated devices along with other essential parameters such as J_{SC}, V_{oc}, and FF are obtained and analyzed in this study.

Figure 6a–d exhibit the $J-V$ characteristics of **1**–**4** TCNQ-based PV devices. The inset of the figure portrays the cross-section of the device structure for all of the fabricated solar cells. It is observed that the aliphatic amine substituent showed a nominal impact on the PV behavior in **2**. Whereas aromatic amines contributed to the optimum conditions leading to considerable device efficiency, furthermore, **1** manifested the highest device efficiency of 11.75%. More strikingly, the J_{SC} of the **1** PV device has increased from 2 mA/cm^2 under dark conditions to 9.12 mA/cm^2 in the presence of light, which is a huge leap in current, almost 4.5 times higher. The films of compounds **1**–**4** exhibited broad and low-energy absorptions, which could be attributed to an intramolecular charge-transfer transition (Figure 1). This characteristic is commonly observed in TCNQ derivatives with amine substitutions.[26] The AFM image of **1** revealed higher crystallinity (Figure 4a), and dense packing is envisaged from the FESEM (Figure 4e) image, beneficial for improving the charge transport. Thus, **1** showed the highest PCE of 11.75%. Likewise, increased crystallinity leads to enhanced mobility, reduced defects, and improved PV performance. Also, crystal structure analysis of **1** revealed supramolecular assembly, H-bonding, and noncovalent interactions.[5] Film of **4** with a monosubstituent aromatic moiety exhibited lesser crystalline features (Figure 4d) displaying PCE as 5.90%. Also, **4** showed $\pi-\pi$ stacking and extensive short contacts in the crystal lattice.[21] The PCE of **3** was found to be 2.58%, less than that of **4**, though **3** also has an aromatic substituent, possibly due to minimal crystallinity (Figure 4c), and the presence of $-CF_3$ and $-CN$ adding an -I effect decreases the π-electron density over the aromatic ring to be available for stacking. Further, the absence of an aromatic ring substituent and the presence of solely aliphatic amine depicts the lowest PCE for **2** (PCE = 2.12%) among **1**–**4**. Thus, the order of PCE followed the trend **1** > **4** > **3** > **2**. The detailed PV performance parameters are listed in Table 1.

The findings presented in Table 1 suggest that parasitic resistive losses, such as current leakages due to pinholes or traps in the thin films, appear to lower the FF for the **3** based PV devices. This may be caused by a combination of factors,

Table 1. PV Device Performance Parameters for Different TCNQ Derivatives 1–4

s. no.	TCNQ derivative	dark (mA)	J_{SC} (mA/cm^2)	V_{oc} (V)	FF	efficiency (%)
1	**1**	2	9.12	3	0.43	11.75
2	**2**	0.4	1.25	3	0.59	2.12
3	**3**	0.7	4.3	3	0.21	2.58
4	**4**	1.4	4.8	3	0.41	5.90

https://doi.org/10.1021/acsomega.3c05939
ACS Omega 2023, 8, 40836–40847

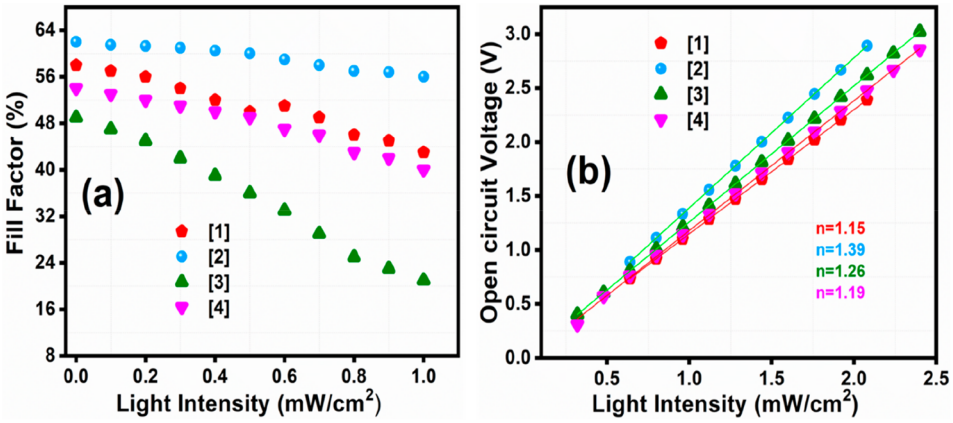

Figure 7. (a) FF as a function of light intensity for all of the synthesized molecules. (b) Influence of light intensity on open circuit voltage for all of the synthesized small molecules.

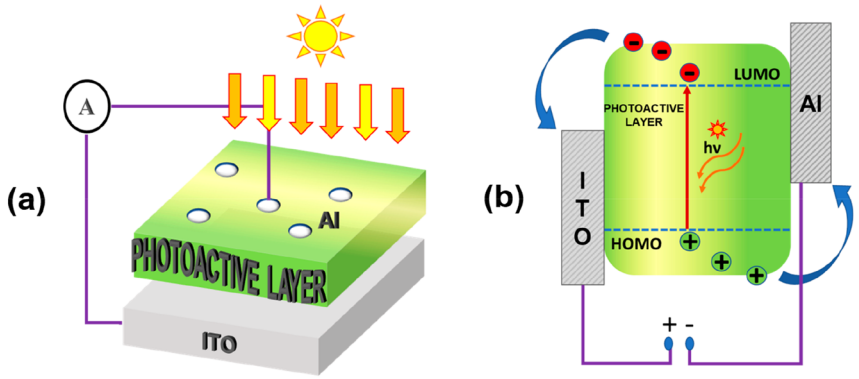

Figure 8. (a) Schematic of the PV device for all four compounds **1**−**4**. (b) The band diagram illustrates the steps involved in generating excitons, separating them into free charge carriers, and then extracting these charge carriers to generate electrical current.

including high series resistance (R_s) due to large resistivity (ρ) in the photoactive layers. Furthermore, the authors discovered a negative correlation between light intensity and FF, as the latter tended to decrease with an increase in light intensity. For instance, the FF of the **1** device decreased from 56 to 43% and stabilized as the light intensity changed from 0.2 to 1 sun. A similar trend was observed for other molecules (as shown in Figure 7a), which suggests that there is a reduction in shunt resistance (R_{SH}) attributed to increased leakage and carrier recombination, as a higher amount of photogenerated carriers was present in the PV devices under high illumination intensity.

To comprehend the impact of the recombination losses mentioned earlier on the device performance, an in-depth investigation of V_{OC} characteristics was conducted under different light intensities. This study aimed to explore the dynamics of the charge carriers within the device. The correlation between V_{OC} and natural logarithm-intensity (I) is commonly represented by the equation $V_{OC} \propto n(kT/q)\ln(I)$, where k denotes the Boltzmann constant, T represents the temperature in Kelvin, and q represents the charge.[41] At constant temperature, the ideality factor (n) in the equation represents the degree of nonideal behavior in the diode equation, which can also affect carrier recombination. The value of n, which can range from 1 to 2, indicates whether trap-free conditions exist ($n = 1$) or if there are charge-carrier traps present to some extent in the device's active layer or at the interface between the active layer and the electrode ($n \neq 1$). Based on the results presented in Figure 7b, it can be inferred that the **1** based PVs experienced lower levels of trap-based recombination compared to the other devices, as evidenced by the fitted n value of 1.15. On the other hand, the **2**, **3**, and **4** devices had higher fitted n values of 1.37, 1.26, and 1.19, respectively, indicating that they suffered from more trap-based recombination. Normally, carrier recombination causes a loss of charge carriers, reducing the overall current and, consequently, the PCE of the solar cell. Recombination takes place through different mechanisms including trap-assisted or surface recombination, which result in the loss of photogenerated carriers before they can contribute to the cell's output. When trap-assisted recombination is prevalent, charge carriers can become trapped at defect sites within the material, leading to their recombination and a reduced current. This recombination process diminishes the PCE because it lowers the number of charge carriers that are accessible for collection. Similarly, surface recombination occurs at the interfaces between the material film and the electrodes. If the interfaces possess defects or inadequate passivation, then charge carriers can recombine at these surfaces instead of contributing to the electrical output. This surface recombination reduces the effective carrier lifetime and diminishes the PCE. To improve the PCE of a solar cell, minimizing the recombination losses is crucial. Enhancing the quality of the semiconductor material, optimizing device design, and implementing effective passivation techniques can help reduce recombination rates and improve the PCE. By mitigating recombination losses, more

https://doi.org/10.1021/acsomega.3c05939
ACS Omega 2023, 8, 40836−40847

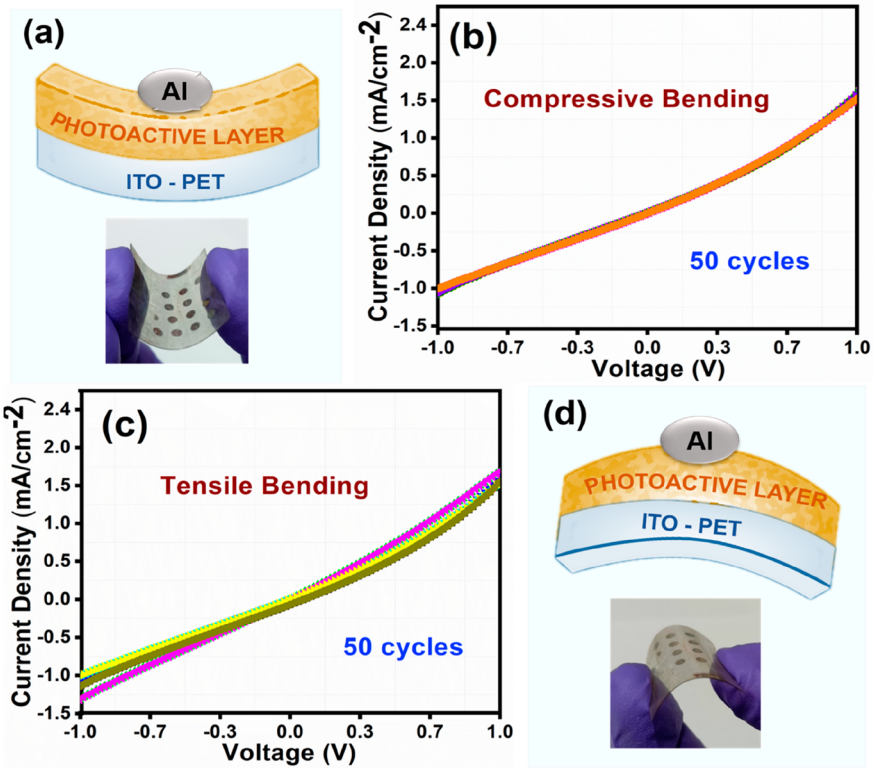

Figure 9. Flexure or bending tests conducted on a fabricated TCNQ-based PV device. (a) Schematic of the device during compressive bending. (b) $J_{SC}-V$ curves measured while subject to compressive stretching. (c) $J_{SC}-V$ curves measured during tensile bending and (d) diagram illustrating the configuration of the device during the application of tensile stretching.

photogenerated charge carriers can be harvested, leading to a higher current and increased PCE of the solar cell.[42]

3.5.1. Band Diagram. To gain deeper insights into the carrier-transport mechanisms within the fabricated PV devices, the properties of charge recombination and collection were investigated under the operating conditions. A significant challenge lies in managing the interpenetrating networks in TCNQ small molecule OSCs, as inefficient charge transport pathways can result in excessive exciton recombination, reduced charge carrier mobility, and imbalanced charge-transport capabilities. To address this issue, a hierarchical morphology offers a promising approach that allows for simultaneous balanced charge separation and charge transport.[33] The PV device structure mainly consists of the **1**, **2**, **3**, and **4** layers each sandwiched between the top Al and the bottom ITO electrodes, Figure 8.

When no light is present, the photoinduced electrons within the active layer produce a relatively weak electric field and experience rapid recombination. As a consequence, this leads to low values of both open circuit voltage (V_{OC}) and short circuit current (J_{SC}) when no external bias is applied.[43] Under light irradiation, however, when a reverse bias is applied, the difference in energy levels between the HOMO and LUMO of the photoactive layers (Table S5) and the electrodes leads to effective band bending and charge separation at the interfaces. An ohmic contact is created at the junction by the bottom ITO, providing the necessary driving force for charge carriers to pass through the interface, thereby enhancing charge extraction and collection efficiency. Likewise, the uppermost aluminum (Al) layer induces band-bending and establishes a Schottky barrier, which hinders recombination at the interface and facilitates the efficient extraction of holes from the active layer.

The wide range of absorption observed in compounds **1**–**4** (Figure 1) is probably a result of intramolecular charge-transfer transitions; a further large bathochromic shift in films in contrast to solutions suggests aggregation of molecules and considerable $\pi-\pi$ stacking, i.e., significant intermolecular interactions. **1**–**4** possess varied functional groups within the molecule that can absorb light at different wavelengths. This results in a higher number of photoinduced carriers being generated within the material especially in **1** followed by **4** and **3**, as they can absorb light over a wider range of the electromagnetic spectrum. On the other hand, **2**'s narrow spectral range with a peak height of 340 nm may limit the number of photoinduced carriers generated within the material. To investigate the superior PV properties of **1** over the other molecules, **2**, **3**, and **4**, the carrier decay lifetime (τ) of all of the synthesized materials was acquired and compared, as it is identified to be a vital factor in limiting the photogenerated current losses. The average transient decay-lifetime characteristics indicated the rate of carrier recombination and charge extraction in these devices. As indicated in Table S4a, rapid decay characteristics were observed for the DMF solutions of **3** followed by **4** with lifetime values of 0.07 and 0.20 ns, respectively, suggesting early recombination of photogenerated electrons and holes in the active region of these PV devices, which agrees with the lower yielding J_{SC} values than those of **1** (Table 1). As conveyed, fluorescence lifetime decay was not unveiled by solids **3** and **4**, probably due to fast excited state relaxation by the nonradioactive decay pathway.

https://doi.org/10.1021/acsomega.3c05939
ACS Omega 2023, 8, 40836−40847

Meanwhile, **1** and **2** exhibited longer lifetime component values of 0.88 and 1.2 ns, respectively. This signifies a much-prolonged lifetime for the photoinduced active e−h pairs, substantiating the presence of trap states in the band gap of these molecules that provide alternative ways for electronic relaxation; as a result, the radiative recombination process is reduced, and there is a substantial delay in the carrier recombination process. This delay in carrier recombination can have significant implications for applications such as solar cells, where it is desirable to extend the lifetime of photoinduced active e−h pairs to increase the efficiency of energy conversion. The presence of trap states in these molecules provides an additional mechanism to extend the lifetime of these active e−h pairs and improve the overall efficiency of the PV devices. Therefore, **1** shows an effective charge extraction capability, thereby efficiently curbing the recombination phenomenon in the PV device contributing to the improvement of FF and the PCE of the device. The lifetime for **2** was observed to be the highest as it is also a fluorescent material; that is, electrons remain in the excited state for a longer time. However, it has a low absorption coefficient, which means that it cannot absorb a significant amount of incident light, which is evident from the UV−vis spectroscopy studies (Figure 1). Consequently, the generation of photoexcited carriers within the material is constrained, leading to a low power conversion efficiency (PCE) despite having a long carrier lifetime. Additionally, the overall processing conditions can also have a significant impact on the PCE. For example, the presence of defects or impurities in the device can lead to carrier trapping and recombination, which can limit the efficiency of the device despite the favorable properties of the fluorescent material itself.[44]

3.5.2. Bending Studies. The PV device demonstrated nearly indistinguishable electrical characteristics during compressive bending, as depicted in Figure 9a,b; when compared to the device bent neutrally and scanned from −1 to +1 V. Even when subject to tensile flexure or downward bending of the PV unit cell, the similarity in characteristics was upheld. Interestingly, a slight increment in current density was noticed at maximum bending, possibly attributed to the abrupt surge in substrate resistance. Nonetheless, upon restoring the device to its original position, the $J-V$ characteristics remained stable, providing further evidence of its robustness (Figure 9c,d). The results affirm the reliability and durability of the device, essential qualities vital to roll-to-roll processing enabling the low-power design of wearable electronics.

4. CONCLUSIONS

Our investigation of di-/monosubstituted TCNQ derivatives with various amine substituents has provided valuable insights into their PV behavior and influenced PCE in **1**−**4**. **1**−**4** themselves played a crucial role as the photoactive layers possessing a donor−acceptor framework. Thus, **1**−**4** suggest their potential application/emergence as all small molecule-based OSCs. Utilization of aminoethyl pyridine in **1** has proven crucial in achieving the highest device efficiency of 11.75%. This enhancement can be attributed to remarkable crystallinity with high roughness (R_q = 19.40 nm) and ordered, dense molecular packing in **1** due to the presence of multiple aromatic pyridine moieties, which promotes effective stacking and extended light absorption, leading to improved current generation. The presence of an ethylene spacer helps in single-bond rotation, therefore improving the charge transport through the ICT process. Considerable crystallinity (R_q = 18.36 nm) with compact $\pi-\pi$ stacking justifies the enhanced PCE (5.90%) of **4**, followed by **3** (PCE = 2.58%, R_q = 14.83 nm); conversely, the absence of an aromatic amine substituent in **2** resulted in the lowest R_q = 8.686 nm and the lowest PCE = 2.12% among **1**−**4**. Higher values of R_q highlight the bigger crystallites predominant in **1** and **4** than those in **3** and **2**. Thus, the higher PCE, single-step synthesis, and cost-effectiveness of the **1** PV device qualify it as a potential candidate for a commercially viable device. However, further efforts should be directed toward improving the FF of the devices. Our previous research has demonstrated that work infusion of the electron transport layer, introducing a compatible functional moiety, and blending with polymers can effectively enhance and achieve a commendable PCE surpassing the current OSCs' efficiencies. To conclude, **1** opens up possibilities for further exploration and optimization of these materials for high-performance OSCs. Importantly, the absolute PCE values (>10%) exceed only those of conventional doped perovskite solar cells (<10%); nevertheless, in this study, **1** could achieve a PCE over 11%. Therefore, the current strategies offer promising opportunities for future research aimed at achieving a higher PCE and advancing the field of TCNQ derivative-based OSCs. By leveraging their enhanced efficiency and stability, TCNQ derivatives can contribute to the advancement of organic PVs and the realization of sustainable and cost-effective solar energy conversion technologies.

■ ASSOCIATED CONTENT

Supporting Information

The Supporting Information is available free of charge at https://pubs.acs.org/doi/10.1021/acsomega.3c05939.

Detailed information on photophysical studies, cyclic voltammetry studies, spectroscopy, crystallographic details of material, device fabrication, and thin film characterization (PDF)

■ AUTHOR INFORMATION

Corresponding Author

Subbalakshmi Jayanty − *Department of Chemistry, Birla Institute of Technology and Science, Pilani-Hyderabad Campus, Hyderabad 500078 Telangana State, India;* orcid.org/0000-0003-0350-694X; Email: jslakshmi@hyderabad.bits-pilani.ac.in

Authors

Anuradha Mohitkar − *Department of Chemistry, Birla Institute of Technology and Science, Pilani-Hyderabad Campus, Hyderabad 500078 Telangana State, India*

Renuka H − *MEMS, Microfluidics and Nanoelectronics Lab, Department of Electrical and Electronics Engineering, Birla Institute of Technology and Science, Hyderabad 500078 Telangana State, India;* Present Address: Postdoctoral Research Associate, Mechanical Department, Carnegie Mellon University, 5000 Forbes Avenue, Pittsburgh, Pennsylvania 15213

Sanket Goel − *MEMS, Microfluidics and Nanoelectronics Lab, Department of Electrical and Electronics Engineering, Birla Institute of Technology and Science, Hyderabad 500078 Telangana State, India;* orcid.org/0000-0002-9739-4178

Complete contact information is available at: https://pubs.acs.org/10.1021/acsomega.3c05939

https://doi.org/10.1021/acsomega.3c05939
ACS Omega 2023, 8, 40836−40847

Notes

The authors declare no competing financial interest.

■ ACKNOWLEDGMENTS

S.J. thanks the University of Hyderabad for providing the AFM and TEM facility. S.J. also thanks the BITS-Pilani Hyderabad campus for financial assistance to A.M. The Central Analytical Laboratory (CAL) facility provided by the BITS-Pilani, Hyderabad campus and the DST-FIST grant facility sanctioned to the Department of Chemistry, BITS-Pilani Hyderabad Campus are also highly acknowledged.

■ REFERENCES

(1) Chandaluri, C. G.; Radhakrishnan, T. P. Zwitterionic Diaminodicyanoquinodimethanes with Enhanced Blue-Green Emission in the Solid State. *Opt. Mater. (Amst).* **2011**, *34* (1), 119−125.
(2) Boyineni, A.; Jayanty, S. Supramolecular Helical Self-Assemblies and Large Stokes Shift in 1-(2-Cyanophenyl)Piperazine and 4-Piperidinopiperidine Bis-Substituted Tetracyanoquinodimethane Fluorophores. *Dyes Pigm.* **2014**, *101*, 303−311.
(3) Jayanty, S.; Radhakrishnan, T. P. Enhanced Fluorescence of Remote Functionalized Diaminodicyanoquinodimethanes in the Solid State and Fluorescence Switching in a Doped Polymer by Solvent Vapors. *Chem.—Eur. J.* **2004**, *10* (3), 791−797.
(4) Radhakrishnan, T. P. Molecular Structure, Symmetry, and Shape as Design Elements in the Fabrication of Molecular Crystals for Second Harmonic Generation and the Role of Molecules-in-Materials. *Acc. Chem. Res.* **2008**, *41* (3), 367−376.
(5) Raghavaiah, P.; Kuladeep, R.; Narayana Rao, D.; Jyothi Lakshmi, A.; Srujana, P.; Subbalakshmi, J. Bis-(1-(2-Aminoethyl)Piperidino), (2-(2-Aminoethyl)Pyridino) and (1-(2-Aminoethyl)Pyrrolidino)-Substituted Dicyanoquinodimethanes: Consequences of Flexible Ethylene Spacers with Heterocyclic Moieties and Amine Functionalities. *Acta. Crystallogr. B. Struct. Sci. Cryst. Eng. Mater.* **2016**, *72* (5), 709−715.
(6) Mohammadtaheri, M.; Ramanathan, R.; Bansal, V. Emerging Applications of Metal-TCNQ Based Organic Semiconductor Charge Transfer Complexes for Catalysis. *Catal. Today* **2016**, *278* (2), 319−329.
(7) Zhu, L.; Chang, H.; Vavallo, C. L.; Jiang, J.; Zeng, Z.; Yang, J.; Smith, M. D.; Miao, S. Synthesis and Properties of Tetracyanoquinodimethane Derivatives. *Heterocycl. Comm.* **2018**, *24* (5), 249−254.
(8) Zhang, Z.; Gou, G.; Wan, J.; Li, H.; Wang, M.; Li, L. Synthesis, Structure, and Significant Energy Gap Modulation of Symmetrical Silafluorene-Cored Tetracyanobutadiene and Tetracyanoquinodimethane Derivatives. *J. Org. Chem.* **2022**, *87* (5), 2470−2479.
(9) Matsuoka, S.; Ogawa, K.; Ono, R.; Nikaido, K.; Inoue, S.; Higashino, T.; Tanaka, M.; Tsutsumi, J.; Kondo, R.; Kumai, R.; Tsuzuki, S.; Arai, S.; Hasegawa, T. Highly Stable and Isomorphic Donor-Acceptor Stacking in a Family of n-Type Organic Semiconductors of BTBT-TCNQ Derivatives. *J. Mater. Chem. C* **2022**, *10* (43), 16471−16479.
(10) Sudhakar, P.; Radhakrishnan, T. P. A Strongly Fluorescent Molecular Material Responsive to Physical/Chemical Stimuli and Their Coupled Impact. *Chem. Asian. J.* **2019**, *14* (24), 4754−4759.
(11) Sudhakar, P.; Radhakrishnan, T. P. Stimuli-Responsive and Reversible Crystalline-Amorphous Transformation in a Molecular Solid: Fluorescence Switching and Enhanced Phosphorescence in the Amorphous State. *J. Mater. Chem. C* **2019**, *7* (23), 7083−7089.
(12) Syed, A.; Battula, H.; Mishra, S.; Jayanty, S. Distinct Tetracyanoquinodimethane Derivatives: Enhanced Fluorescence in Solutions and Unprecedented Cation Recognition in the Solid State. *ACS Omega.* **2021**, *6* (4), 3090−3105.
(13) Senthilnathan, N.; Radhakrishnan, T. P. Molecular Hopper Crystals and Electron Beam-Triggered Reversible Actuation. *Chem. Mater.* **2020**, *32* (19), 8567−8575.
(14) Zhang, L.; Zhu, X.; Deng, D.; Wang, Z.; Zhang, Z.; Li, Y.; Zhang, J.; Lv, K.; Liu, L.; Zhang, X.; Zhou, H.; Ade, H.; Wei, Z. High Miscibility Compatible with Ordered Molecular Packing Enables an Excellent Efficiency of 16.2% in All-Small-Molecule Organic Solar Cells. *Adv. Mater.* **2022**, *34* (5), 2106316.
(15) Ge, J.; Hong, L.; Ma, H.; Ye, Q.; Chen, Y.; Xie, L.; Song, W.; Li, D.; Chen, Z.; Yu, K.; Zhang, J.; Wei, Z.; Huang, F.; Ge, Z. Asymmetric Substitution of End-Groups Triggers 16.34% Efficiency for All-Small-Molecule Organic Solar Cells. *Adv. Mater.* **2022**, *34* (29), 2202752.
(16) Mishra, A.; Sharma, G. D. Harnessing the Structure-Performance Relationships in Designing Non-Fused Ring Acceptors for Organic Solar Cells. *Angew. Chem., Int. Ed.* **2023**, *62* (21), No. e202219245.
(17) Yao, H.; Hou, J. Recent Advances in Single-Junction Organic Solar Cells. *Angew. Chem., Int. Ed.* **2022**, *61* (37), No. e202209021.
(18) Paci, I.; Johnson, J. C.; Chen, X.; Rana, G.; Popović, D.; David, D. E.; Nozik, A. J.; Ratner, M. A.; Michl, J. Singlet Fission for Dye-Sensitized Solar Cells: Can a Suitable Sensitizer Be Found? *J. Am. Chem. Soc.* **2006**, *128* (51), 16546−16553.
(19) Liu, C.; Li, Z.; Zhang, Z.; Zhang, X.; Shen, L.; Guo, W.; Zhang, L.; Long, Y.; Ruan, S. Improving the Charge Carrier Transport of Organic Solar Cells by Incorporating a Deep Energy Level Molecule. *Phys. Chem. Chem. Phys.* **2017**, *19* (1), 245−250.
(20) Jayanty, S.; Gangopadhyay, P.; Radhakrishnan, T. P. Steering Molecular Dipoles from Centrosymmetric to a Noncentrosymmetric and SHG Active Assembly Using Remote Functionality and Complexation. *J. Mater. Chem.* **2002**, *12* (9), 2792−2797.
(21) Syed, A.; Battula, H.; Bobde, Y.; Patel, T.; Ghosh, B.; Jayanty, S. Design and Development of Distinct Tetracyanoquinodimethane Derivatives Exhibiting Dual Effect of Fluorescence and Anticancer Activity. *Chemistry Select* **2021**, *6* (29), 7354−7366.
(22) Kumar, A.; Shkir, M.; Somaily, H. H.; Singh, K. L.; Choudhary, B. C.; Tripathi, S. K. A Simple, Low-Cost Modified Drop-Casting Method to Develop High-Quality $CH_3NH_3PbI_3$ Perovskite Thin Films. *Physica. B Condens. Matter.* **2022**, *630*, 413678.
(23) Zuo, C.; Ding, L. Drop-Casting to Make Efficient Perovskite Solar Cells under High Humidity. *Angew. Chem., Int. Ed.* **2021**, *60* (20), 11242−11246.
(24) Rajanna, P. M.; Gilshteyn, E. P.; Yagafarov, T.; Aleekseeva, A. K.; Anisimov, A. S.; Neumüller, A.; Sergeev, O.; Bereznev, S.; Maricheva, J.; Nasibulin, A. G. Enhanced Efficiency of Hybrid Amorphous Silicon Solar Cells Based on Single-Walled Carbon Nanotubes and Polymer Composite Thin Film. *Nanotechnology* **2018**, *29* (10), 105404.
(25) Patra, A.; Hebalkar, N.; Sreedhar, B.; Sarkar, M.; Samanta, A.; Radhakrishnan, T. P. Tuning the Size and Optical Properties in Molecular Nano/Microcrystals: Manifestation of Hierarchical Interactions. *Small* **2006**, *2* (5), 650−659.
(26) Patra, A.; Radhakrishnan, T. P. Molecular Materials with Contrasting Optical Responses from a Single-Pot Reaction and Fluorescence Switching in a Carbon Acid. *Chem.—Eur. J.* **2009**, *15* (12), 2792−2800.
(27) Bloor, D.; Kagawa, Y.; Szablewski, M.; Ravi, M.; Clark, S. J.; Cross, G. H.; Pålsson, L. O.; Beeby, A.; Parmer, C.; Rumbles, G. Matrix Dependence of Light Emission from TCNQ Adducts. *J. Mater. Chem.* **2001**, *11* (12), 3053−3062.
(28) Lakowicz, J. R. *Principles of Fluorescence Spectroscopy*, 3rd ed.; Springer: Boston, MA, 2006.
(29) Perepichka, D. F.; Bryce, M. R.; Pearson, C.; Petty, M. C.; McInnes, E. J. L.; Zhao, J. P. A Covalent Tetrathiafulvalene-Tetracyanoquinodimethane Diad: Extremely Low HOMO-LUMO Gap, Thermoexcited Electron Transfer, and High-Quality Langmuir-Blodgett Films. *Angew. Chem., Int. Ed.* **2003**, *42* (38), 4636−4639.
(30) Keshtov, M. L.; Kuklin, S. A.; Radychev, N. A.; Nikolaev, A. Y.; Ostapov, I. E.; Krayushkin, M. M.; Konstantinov, I. O.; Koukaras, E. N.; Sharma, A.; Sharma, G. D. New Low Bandgap Near-IR Conjugated D-A Copolymers for BHJ Polymer Solar Cell Applications. *Phys. Chem. Chem. Phys.* **2016**, *18* (12), 8389−8400.
(31) Syed, A.; H, R.; Mohitkar, A.; Pallepogu, R.; Challa, M. S. K.; Goel, S.; Jayanty, S. Photophysical, Electrochemical Properties and Flexible Organic Solar Cell Application of 7,7-Bis(1-Cyclopropyl

https://doi.org/10.1021/acsomega.3c05939
ACS Omega 2023, 8, 40836−40847

Carbonyl Piperazino)-8,8 Dicyanoquinodimethane. *Mater. Adv.* **2022**, *3* (7), 3151−3164.
(32) Halder, S.; Behere, R. P.; Gupta, N.; Kuila, B. K.; Chakraborty, C. Enhancement of the Electrochemical Performance of a Cathodically Coloured Organic Electrochromic Material through the Formation of Hydrogen-Bonded Supramolecular Polymer Assembly. *Sol. Energy Mater. Sol. Cells.* **2022**, *245*, 111858.
(33) Zhou, R.; Jiang, Z.; Yang, C.; Yu, J.; Feng, J.; Adil, M. A.; Deng, D.; Zou, W.; Zhang, J.; Lu, K.; Ma, W.; Gao, F.; Wei, Z. All-Small-Molecule Organic Solar Cells with over 14% Efficiency by Optimizing Hierarchical Morphologies. *Nat. Commun.* **2019**, *10* (1), 132921.
(34) Pan, L.; Liu, T.; Wang, J.; Ye, L.; Luo, Z.; Ma, R.; Pang, S.; Chen, Y.; Ade, H.; Yan, H.; Duan, C.; Huang, F.; Cao, Y. Efficient Organic Ternary Solar Cells Employing Narrow Band Gap Diketopyrrolopyrrole Polymers and Nonfullerene Acceptors. *Chem. Mater.* **2020**, *32* (17), 7309−7317.
(35) Sidhik, S.; Pasarán, A. C.; Rosiles Pérez, C.; López-Luke, T.; De La Rosa, E. Modulating the Grain Size, Phase and Optoelectronic Quality of Perovskite Films with Cesium Iodide for High-Performance Solar Cells. *J. Mater. Chem. C* **2018**, *6* (29), 7880−7889.
(36) Jehl, Z.; Bouttemy, M.; Lincot, D.; Guillemoles, J. F.; Gerard, I.; Etcheberry, A.; Voorwinden, G.; Powalla, M.; Naghavi, N. Insights on the Influence of Surface Roughness on Photovoltaic Properties of State of the Art Copper Indium Gallium Diselenide Thin Films Solar Cells. *J. Appl. Phys.* **2012**, *111* (11), 114059.
(37) Liu, P.; Huang, B.; Peng, L.; Liu, L.; Gao, Q.; Wang, Y. A Crack Templated Copper Network Film as a Transparent Conductive Film and Its Application in Organic Light-Emitting Diode. *Sci. Rep.* **2022**, *12* (1), 20494.
(38) Renuka, H.; Enaganti, P. K.; Kundu, S.; Goel, S. Laser-Induced Graphene Electrode Based Flexible Heterojunction Photovoltaic Cells. *Microelectron. Eng.* **2022**, *251*, 111673.
(39) Qi, B.; Wang, J. Fill factor in organic solar cells. *Phys. Chem. Chem. Phys.* **2013**, *15*, 8972−8982.
(40) Zhang, X.; Li, C.; Xu, J.; Wang, R.; Song, J.; Zhang, H.; Li, Y.; Jing, Y. N.; Li, S.; Wu, G.; Zhou, J.; Li, X.; Zhang, Y.; Li, X.; Zhang, J.; Zhang, C.; Zhou, H.; Sun, Y.; Zhang, Y. High Fill Factor Organic Solar Cells with Increased Dielectric Constant and Molecular Packing Density. *Joule* **2022**, *6* (2), 444−457.
(41) Duan, T.; Chen, Q.; Yang, Q.; Hu, D.; Cai, G.; Lu, X.; Lv, J.; Song, H.; Zhong, C.; Liu, F.; Yu, D.; Lu, S. Simple Thiazole-Centered Oligothiophene Donor Enables 15.4% Efficiency All Small Molecule Organic Solar Cells. *J. Mater. Chem. A* **2022**, *10* (6), 3009−3017.
(42) Kirchartz, T.; Nelson, J. In *Multiscale Modelling of Organic and Hybrid Photovoltaics*; Beljonne, D., Cornil, J., Eds.; Topics in Current Chemistry; Springer: Berlin, 2014; vol *352*, Chapter 7, pp 279324.
(43) Renuka, H.; Joshna, P.; Venkataraman, B. H.; Ramaswamy, K.; Kundu, S. Understanding the Efficacy of Electron and Hole Transport Layers in Realizing Efficient Chromium Doped BiFeO3 Ferroelectric Photovoltaic Devices. *Sol. Energy* **2020**, *207*, 767−776.
(44) Hu, D.; Tang, H.; Karuthedath, S.; Chen, Q.; Chen, S.; Khan, J. I.; Liu, H.; Yang, Q.; Gorenflot, J.; Petoukhoff, C. E.; Duan, T.; Lu, X.; Laquai, F.; Lu, S. A Volatile Solid Additive Enables Oligothiophene All-Small-Molecule Organic Solar Cells with Excellent Commercial Viability. *Adv. Funct. Mater.* **2023**, *33* (6), 2211873.

https://doi.org/10.1021/acsomega.3c05939
ACS Omega 2023, 8, 40836−40847